

Discontinuous Tension-Controlled Transition between Collective Actuations in Active Solids

Paul Baconnier^{1,†}, Dor Shohat^{1,2}, and Olivier Dauchot^{1,*}

¹UMR CNRS Gulliver 7083, ESPCI Paris, PSL Research University, 75005 Paris, France

²School of Physics and Astronomy, Tel-Aviv University, Tel Aviv 69978, Israel

(Received 19 August 2022; revised 10 October 2022; accepted 21 December 2022; published 11 January 2023)

The recent finding of collective actuation in active solids—solids embedded with active units—is a new promise for the design of multifunctional materials with genuine autonomy, and a better understanding of dense biological systems. Here, we combine the experimental study of centimetric model active solids, the numerical study of an agent-based model, and theoretical arguments to reveal a new form of collective actuation and how mechanical tension can serve as a general mechanism for transitioning between different collective actuation regimes. The presence of hysteresis when varying tension back and forth highlights the nontrivial selectivity of collective actuations.

DOI: 10.1103/PhysRevLett.130.028201

Active solids are dense assemblies or elastic structures made of—or doped with—active units. They encompass a wide class of systems ranging from biological to manmade materials [1–14]. Collective actuation (CA) takes place when spontaneous activation of a few harmonic modes occurs, and was first reported in a numerical study of jammed active particles [2]. More recently, the experimental realization and theoretical study of CA in stable elastic structures [14] has demonstrated the key role of nonlinear elasto-active feedback between the deformations of the structure and the orientations of the active units. A typical realization of CA is illustrated in Fig. 1. When an active elastic structure, to be further described below, is pinned at its edges, its nodes perform a synchronized chiral oscillation (SCO) around their reference positions [Fig. 1(b); Supplemental Material, Movie 1 [15]].

Very similar SCO dynamics have been reported in confined epithelial cells [20] and dense bacterial suspensions [21,22]. Another collective dynamics, with the system performing global alternating rotation (GAR) around its center, was even reported in biofilms [22,23], and, quite remarkably, a transition from SCO to GAR could be observed as activity decreases [22]. From a biomimetic point of view, active metamaterials are therefore a promising framework for creating multifunctional materials [24–28] with bona fide autonomy [29]. An explicit realization of active metamaterials exhibiting different CA regimes, with a good control on the transition between these regimes is however still lacking.

In this Letter, we bridge this gap by (i) demonstrating the existence of both SCO and GAR in the same active elastic structure, [Figs. 1(a) and 1(b) and Supplemental Material Movies 1 and 2 [15]] and (ii) showing how mechanical tension can be harnessed to control the transition between these different CA regimes. We first

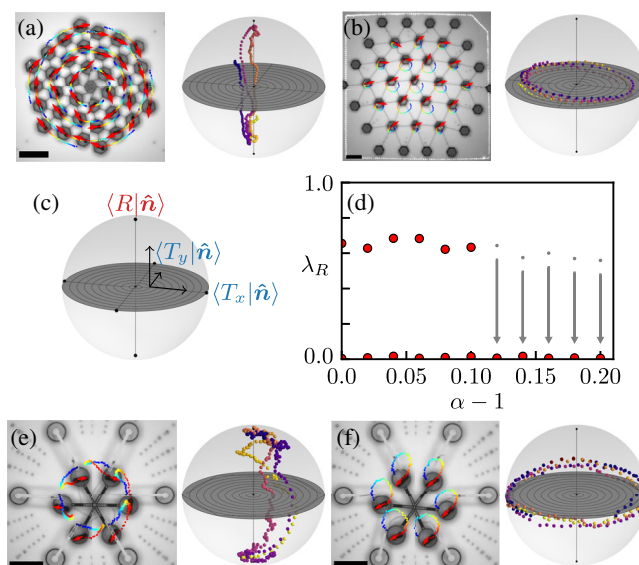


FIG. 1. Experimental realization of a controlled discontinuous transition between collective actuations. (a) GAR in a triangular lattice under central pinning; $N = 36$. (b) SCO in a triangular lattice under edge pinning; $N = 19$. Left panel: dynamics in real space (red arrows, polarities \hat{n} ; trajectories color-coded from blue to red with increasing time; scale bars, 10 cm). Right panel: dynamics projected on the translation and rotation modes of the structures (vertical axis, $\langle R | \hat{n} \rangle$; equatorial plane, $\langle T_{x/y} | \hat{n} \rangle$; see notations and convention in panel (c)). (d) A discontinuous transition between GAR and SCO is obtained in a model elastic structure, the active Gerris, by tuning tension (see also the Supplemental Material, Movie 5 [15]): condensation fraction on the rotation mode λ_R as a function of tension $\alpha - 1$ (red bullets are obtained from data averaged in the steady state; the gray dots and arrows sketch the transitory regime when initial conditions enforce rotation at large tension). (e), (f) GAR, respectively (resp.) SCO in the active Gerris at low ($\alpha = 1.0$), resp. large ($\alpha = 1.8$) tension; $N = 6$.

establish the experimental proof of concept using a toy-model active solid [Figs. 1(e) and 1(f) and Supplemental Material Movies 3 and 4 [15]]. We then dissect the underlying mechanism and extend our findings to more general geometries, on the basis of an agent's model and theoretical arguments. Apart from being a simple design principle, tension control is of significant biological interest, as it is known to play a key role in growth processes and mechanical responses [30–34], especially during morphogenesis.

Our prototypic active solids, described in detail in Ref. [14], consist of elastic structures, composed of N active units connected by coil springs of stiffness k and rest length l_0 (Fig. 1). Each active unit is made of a Hexbug[®], a centimetric battery-powered running robot, embedded in a 3D printed annulus (height 1.4 cm; internal radius 2.5 cm, 3 mm thick). Each active unit exerts a polar force $F_0 \hat{n}_i$, where \hat{n}_i denotes the orientation of the Hexbug. Each node has a well-defined reference position, but is displaced by the active unit. In contrast, the polarity of each unit is free to rotate and reorients toward the node's displacement rate $\dot{\mathbf{u}}_i$ according to a self-alignment mechanism, first identified for walking discs [35], and best illustrated by the dynamics of a Hexbug in a harmonic potential [14,36]. This nonlinear elasto-active feedback between deformations and polarities is controlled by the ratio $\pi = l_e/l_a$ with $l_e = F_0/k$, the typical elastic deformation caused by the active force and l_a , the alignment length over which \hat{n}_i aligns toward $\dot{\mathbf{u}}_i$. π is defined at the microscopic, Hexbug level, and is therefore independent of the boundary condition. When π increases, the dynamics of a triangular elastic lattice, pinned at its edges, exhibit a transition from a disordered noise-dominated regime to the SCO dynamics illustrated in Fig. 1(b), where each node oscillates synchronously around its mechanical equilibrium position [14]. Altogether the dynamics are well described by

$$\dot{\mathbf{u}}_i = \pi \hat{n}_i + \mathbf{F}_i^{\text{el}}, \quad (1a)$$

$$\dot{\hat{n}}_i = (\hat{n}_i \times \dot{\mathbf{u}}_i) \times \hat{n}_i + \sqrt{2D} \xi_i \hat{n}_i^\perp, \quad (1b)$$

where \mathbf{F}_i^{el} is the sum of the elastic forces acting on node i , and ξ_i are random Gaussian variables with zero mean and correlations $\langle \xi_i(t) \xi_j(t') \rangle = \delta_{ij} \delta(t - t')$. The analysis of this model has shown that CA obeys a nontrivial selection mechanism: the dynamics does not necessarily condense on the lowest energy modes of the structure [14].

Our first, simple but important, result is that the GAR regime is readily obtained in the same active network of springs by changing the boundary conditions: when a given node of the elastic structure is pinned both in translation and rotation, the structure alternatively rotates clockwise and counterclockwise around this node [Fig. 1(a) and Supplemental Material, Movie 2 [15]]. As we shall now see, applying tension at the boundary allows for

transitioning abruptly between the SCO and GAR regimes, while keeping π constant. We design a toy-model active elastic structure, which consists of $N = 6$ active units at the vertices of an inner rigid hexagon, each connected radially to the vertices of an outer pinned hexagon via soft springs of stiffness $k = 1$ N/m [Fig. 2(a)]. We term this structure the active *Gerris* in reference to the water strider bug. Tension is controlled by a stepwise elongation of the radial springs by a factor of α . At low tension, the GAR and SCO regimes are both stable [Fig. 1(e) and Supplemental Material, Movie 3 [15]]. At large tension, only the SCO regime is stable, while the GAR regime is metastable [arrows in Fig. 1(d) and Supplemental Material, Movie 4 [15]], allowing for a one-way transition from GAR to SCO (Supplemental Material, Movie 5 [15]).

These dynamics are best described when decomposed on the elastic modes of the structure, that are the eigenvectors $|\varphi_k\rangle$, associated with the eigenvalues ω_k^2 of the dynamical matrix \mathbb{M} . More specifically, we represent the dynamics in the space spanned by the amplitude of the polarity field projected on three modes of interest: the vertical axis represents the normalized projection on the rotation mode $a_R = \langle \mathbf{R} | \hat{n} \rangle / \sqrt{N}$, whereas the equatorial plane represents the normalized projections on the two translational-like modes $a_{T_{x/y}} = \langle T_{x/y} | \hat{n} \rangle / \sqrt{N}$ [Fig. 1(c)]. From the polarity field normalization, the projections are confined inside the three-sphere of radius \sqrt{N} , normalized to 1. In the GAR regime, obtained from the central pinning condition, the dynamics alternatively condensate on the clockwise and counterclockwise rotation (the poles of the sphere), separated by fast reversal motion [Fig. 1(a)]. In the SCO regime, obtained from the edge pinning condition, the dynamics condensate on the translational modes spanning the equator of the sphere [Fig. 1(b)]. Figures 1(e) and 1(f) convincingly demonstrate that the active *Gerris* explores the same dynamics under the control of tension. The dynamics are quantified by the mean square projection of the polarity field on each mode:

$$\lambda_k = \langle a_k^2 \rangle_t = \frac{1}{T} \int^T \left[\frac{\langle \varphi_k | \hat{n}(t) \rangle}{\sqrt{N}} \right]^2 dt. \quad (2)$$

The discontinuous transition from GAR to SCO in the active *Gerris* is illustrated by the abrupt drop of this condensation fraction on the rotation mode λ_R as tension increases [Fig. 1(d)].

We investigate numerically the transition in the active *Gerris*, using Eq. (1). We set $\pi = 2.0$, a value consistent with previous calibrations [14], and investigate the effect of tension. The *Gerris* has six nodes that are connected by a structure, which can safely be considered rigid [Fig. 2(a) and Supplemental Material [15]]. It is thus described by three degrees of freedom, the spatial coordinates of its barycenter and its angular orientation, the dynamical equations which are provided in the Supplemental

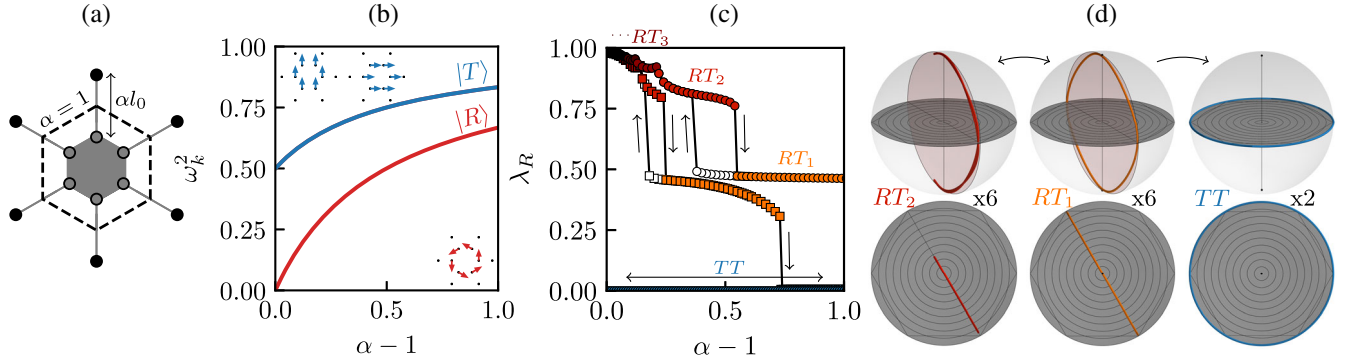


FIG. 2. Active *Gerris*'s dynamics as a function of lattice tension. (a) Elastic architecture cartoon. In gray, the rigid inner hexagon. (b) Normal modes spectrum as a function of springs tension $\alpha - 1$. The red (resp. blue) solid line corresponds to the rotation mode (resp. degenerated translational modes). (c) Condensation fraction on the rotation mode λ_R as a function of lattice tension $\alpha - 1$ (yellow-orange to black symbols, the different *RT* regimes; blue symbols, *TT* regimes; \circ), harmonic approximation; (\square), including geometrical nonlinearities; empty markers, backward annealing). (d) Side and top view of the 3D representations of the polarity field steady dynamics projected on the rotation and translation modes for the regimes *RT*₂ (left), *RT*₁ (middle), and *TT* (right) (vertical axis, $\langle R|\hat{n}\rangle$; equatorial plane, $\langle T_{x/y}|\hat{n}\rangle$).

Material [15]. The three associated normal modes are two degenerated translation modes $|T_{x/y}\rangle$ and one rotation mode $|R\rangle$, which are illustrated in Fig. 2(b), together with their energies as a function of the imposed tension. Both the rotation and translation energies increase with tension, but the energetic ordering of the modes is preserved, and their geometries are unaffected. The three modes end up degenerated at infinite tension.

We first simulate the noiseless, $D = 0$, active *Gerris* equations in the *harmonic approximation*, annealing back and forth between small and large tensions. We find two linearly stable actuation branches, which we denote the *TT* and *RT* regimes [Fig. 2(c), circle markers]. The *TT* regime is a strict condensation of the polarity field on the equator [Fig. 2(d)], with $\lambda_R = 0$, corresponding to a SCO of the *Gerris*. As the dynamics can be restricted to two modes that are degenerated, fully delocalized, and locally orthogonal, this regime exactly maps to that of a single particle trapped in a parabolic potential [14,15,36] (Appendix). The *RT* regimes consist of a condensation of the polarity field on a plane, defined by the rotation vector $|R\rangle$ and one of the six translational vectors $|T\rangle$, pointing toward one of the hexagon's main axes, in the equatorial plane [Fig. 2(d)]. They correspond to a GAR of the *Gerris*. The six possible orientations of this plane define six equivalent attractors, one of which is selected, spontaneously breaking the sixfold symmetry of the system [15]. Depending on the tension, we actually report different *RT* dynamics, separated by hysteretic transitions, which differ in the precise trajectory of the alternating rotation. These *RT* regimes and the transitions among them are well captured by the dynamics of a single particle trapped in elliptic harmonic potentials [15,37] (Appendix). Within the linear level of description, there is however no transition between the coexisting *RT* and *TT* regimes. Including the geometrical nonlinearities of the elastic forces [Fig. 2(c), square

markers], we find that the *TT* regime is unaffected, while the stability ranges of the *RT* regimes are shifted toward smaller tensions. More significantly, the *RT* regime destabilizes toward the *TT* regime for large enough tension. We thus find that geometrical nonlinearities allow for an irreversible and discontinuous transition from the *RT* to the *TT* regime as tension increases.

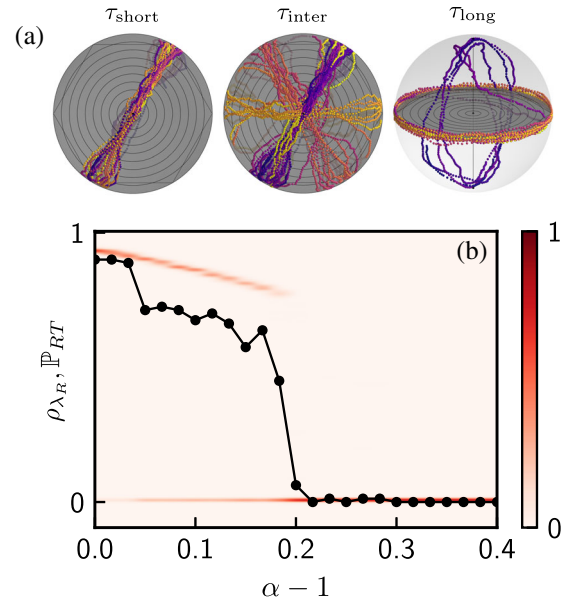


FIG. 3. Active *Gerris*'s dynamics in the presence of noise. (a) Projection of the polarity field dynamics illustrating the effect of noise on the *RT*₁ regime, at short, intermediate, and long times (vertical axis, $\langle R|\hat{n}\rangle$; equatorial plane; $\langle T_{x/y}|\hat{n}\rangle$). (b) Density of condensation fraction on the rotation mode ρ_{λ_R} (color coded as given by the colorbar) and probability of ending up in a *RT* regime at long times \mathbb{P}_{RT} (black markers) as a function of tension $\alpha - 1$.

The TT regime persists for all values of the tension and coexists with the RT regime. We discuss the relative stability of the two attractors by adding a small noise, $D = 10^{-2}$, consistent with existing calibrations [14]. Starting from the RT regime, the system first remains close to the initial RT attractor, then visits the six equivalent RT attractors, before it eventually destabilizes into the TT regime at long times [Fig. 3(a)]. The smaller the tension, the longer it takes for this destabilization to take place. We evaluate the metastability of the RT regime, by simulating 80 independent runs with random initial condition, for each value of the tension. At small tension, the probability of ending up in a RT regime at $t = 10\,000$, \mathbb{P}_{RT} , is close to 1 and slowly decreases with increasing tension. This is due to both the increasing size of the attraction basin of the TT regime and the decreasing lifetime of the metastable RT regime. For tensions $\alpha \geq 1.2$, \mathbb{P}_{RT} vanishes abruptly: all initial conditions end up in the TT regime at long time.

Altogether the active *Gerris* establishes the proof of concept for the experimental control of CA using tension. Its structure, which results from several experimental compromises, is however admittedly rather artificial, raising the question of the possible generalization of the above results to a genuine active material. We theoretically show below that a tension-controlled transition to SCO is generically expected even in the harmonic approximation. Consider an arbitrary lattice undergoing homogeneous dilation of factor $\alpha \in [1, +\infty]$, the dynamical matrix of which reads as [15]

$$\mathbb{M}(\alpha) = \frac{1}{\alpha} \mathbb{M}_0 + \left(1 - \frac{1}{\alpha}\right) \mathbb{M}_1. \quad (3)$$

\mathbb{M}_0 is the dynamical matrix of the structure at zero tension, and \mathbb{M}_1 reads as

$$\mathbb{M}_1 = \begin{pmatrix} \mathbb{M}_1^{xx} & 0 \\ 0 & \mathbb{M}_1^{yy} \end{pmatrix}, \quad (4)$$

where $\mathbb{M}_1^{xx} = \mathbb{M}_1^{yy}$ is the Laplacian matrix of the structure network $\mathbb{M}_{1,ii}^{\alpha\alpha} = Z(i)$, $\mathbb{M}_{1,ij}^{\alpha\alpha} = -1$ if i and j are neighbors and zero otherwise. Since \mathbb{M}_1 decouples the x and y directions, its eigenvectors φ_n come in degenerated pairs with identical form, respectively polarized along x and y . In particular, as a result of a discrete nodal domain theorem [15,38–40], the lowest energy modes of \mathbb{M}_1 have the geometry of translational modes. Increasing the tension, the spectral properties of \mathbb{M}_1 progressively dictate that of the elastic structure, thereby favoring the emergence of two degenerated low-energy modes, with geometries akin to translation. These are the perfect conditions for selecting the SCO regime at large tension [14]. This is why any elastic structure, which, in the absence of tension, exhibits some form of CA, different from the condensation on modes akin to translation, will eventually transition to the SCO regime when tension is increased. This argument is strictly valid in

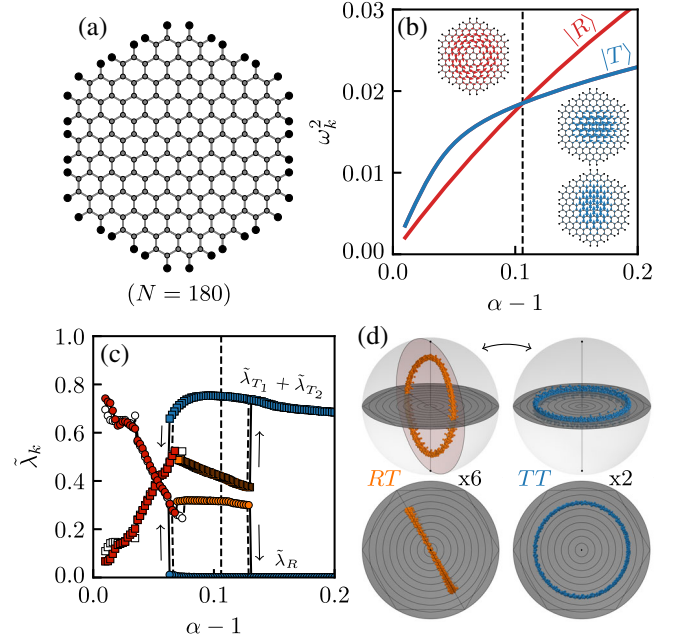


FIG. 4. Active honeycomb's dynamics as a function of lattice tension. (a) Elastic architecture cartoon ($N = 180$). (b) Normal modes' spectrum as a function of lattice tension $\alpha - 1$. The red (resp. blue) solid line corresponds to the rotation mode (resp. degenerated translational modes); see the Supplemental Material [15] for the full spectrum. The dashed black vertical line highlights the crossing of energies. (c) Normalized condensation fractions on the rotation mode $\tilde{\lambda}_R$ (circles) and on the translational modes $\tilde{\lambda}_{T_1} + \tilde{\lambda}_{T_2}$ (squares) as a function of lattice tension $\alpha - 1$. Colored markers and solid lines (resp. white markers and dashed lines) stand for simulations performed within the harmonic approximation (resp. including geometrical nonlinearities). The dark red (resp. orange) branch represents the aperiodic (resp. periodic RT) GAR regime, while the blue branches represent the TT regime. (d) Projection of the polarity field dynamics in the steady states for the RT (left) and TT (right) regime (vertical axis, $\langle R|\hat{n}\rangle$; equatorial plane, $\langle T_{x/y}|\hat{n}\rangle$).

the case of a homogeneous dilation, but one expects it to persist as a design principle for transition between CA in elastic structures which do not dilate homogeneously, as long as tension is evenly distributed. In the case of the *Gerris*, the inner ring is rigid, the dilation is thus not homogeneous, and Eq. (3) does not apply. Would it hold, the two branches of eigenfrequencies, corresponding to the translation and rotation modes meet at infinite tension, and one would expect a transition at infinite α . We however saw that the nonlinearities enforce it at tensions that can be reached experimentally.

We confirm this design principle by considering a large honeycomb lattice, composed of $N = 180$ nodes, pinned at its hexagonal edges [Fig. 4(a)]. Under small tension this lattice has a rotation mode $|R\rangle$ that lies at the bottom of its vibrational spectrum [Fig. 4(b)]. As tension increases, the energies of both the degenerated translational modes and

the rotation mode increase, but at different paces, and eventually cross each other for $\alpha = \alpha_c \simeq 1.1$, as expected from Eq. (3). When simulating the dynamics of the active honeycomb, *within the harmonic approximation*, with $\pi = 0.055$, we do confirm the presence of a discontinuous tension-controlled transition between two linearly stable actuation regimes, SCO and GAR [Fig. 4(c)]. Here, the dynamics condense on modes that are not fully delocalized, thus the condensation fractions are normalized by the participation ratio of the modes $\tilde{\lambda}_k = \lambda_k/Q_k$, with $Q_k = (\sum_i |\phi_k^i|)^2/N$ [15,41].

The SCO is a *TT* regime, very similar to the one discussed above [Fig. 4(d) and Supplemental Material Movie 6 [15]], except for additional fluctuations taking place outside of the equatorial plane. Indeed, the translational modes being not fully delocalized, there is room for a spatial coexistence of a collectively actuated region at the center of the system with a frozen-disordered one close to the boundary [14]. The GAR regimes, with strictly positive $\tilde{\lambda}_R$, exhibit richer dynamics than in the case of the *Gerris*: for small enough tension, the GAR regimes are aperiodic, because of the many low-energy modes, which couple to the rotational and translational modes [15]. At large enough tension, one recovers the *RT*₁ regime, condensed on a *RT* plane in mode space [Fig. 4(d) and Supplemental Material, Movie 7 [15]], modulo some fluctuations of the same origin as in the *TT* regime. Annealing from small to large tension, the *RT* regime transitions to the *TT* one for a tension $\alpha > \alpha_c$ [Fig. 4(c)]. Additionally, performing the backward annealing, the *TT* branch becomes unstable for a tension $\alpha < \alpha_c$. In the absence of geometrical nonlinearities, the observed hysteretic transition must be attributed to the nontrivial selectivity of CA [14]: CA preferably takes place on a pair of modes that are maximally extended and locally orthogonal. As demonstrated by the open symbols and dashed lines in Fig. 4(c), geometrical nonlinearities do not alter the above picture.

On the metamaterial science side, our Letter demonstrates the existence of a generic mechanism for discontinuous transitions between different actuation branches. In the realm of biophysics, it sheds light on the emergence of SCO and GAR regimes, and offers an explanation for the transition observed, when contractility or confinement generates internal stresses.

We thank Yoav Lahini for useful discussions. We acknowledge financial support from Ecole Doctorale ED564 ‘‘Physique en Ile de France’’ for P. B.’s Ph.D. grant. D. S. was supported by a Chateaubriand fellowship.

Appendix: Mapping the active Gerris’s regimes onto single particle dynamics in harmonic potentials.—The active *Gerris*’s *TT* regime [Fig. 2(d)] is a strict condensation of the active dynamics on the two translational modes. This is possible because the translational modes are fully delocalized $Q_{T_x} = Q_{T_y} = 1$,

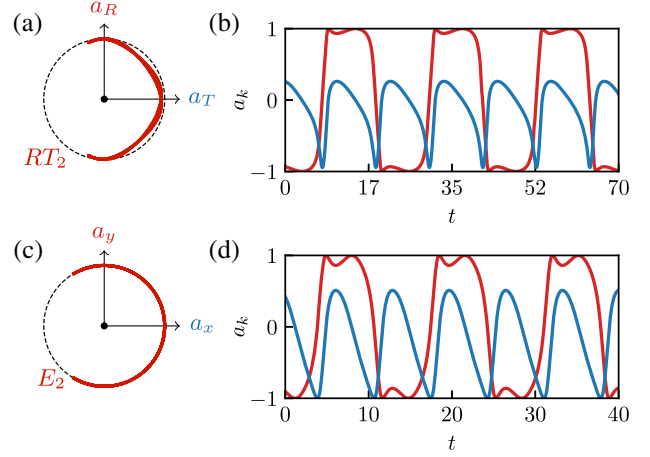


FIG. 5. Mapping between the active *Gerris*’s *RT* regimes and the dynamics of a single particle trapped in an elliptic harmonic potential. Illustration in the case of regimes *RT*₂ \leftrightarrow *E*₂. (a),(b) Active *Gerris*’s *RT*₂ regime ($\alpha = 1.4$); see Fig. 2(d). Polarity field dynamics, restricted to the plane of the two selected modes (a), and as a function of time (b). The solid red (resp. solid blue) line represents a_R (resp. a_T , where T refers to the linear combination of the two translational modes giving the orientation of the plane in Fig. 2(d)). *E*₂ dynamics of a single particle trapped in an elliptic harmonic potential, softer along the y direction ($\omega_x^2 = 1.0$, $\omega_y^2 = 0.36$). Polarity field dynamics in the x - y plane (a), and as a function of time (b). The solid red (resp. solid blue) line represents a_y (resp. a_x). In (a),(c), the dashed black circle represents the unit circle.

and locally orthogonal. Because they also are degenerated, the *TT* regime strictly maps onto the spontaneous oscillation of a single particle in a symmetric parabolic potential [14,15,36]. All quantities of interest can be calculated analytically, e.g., its oscillation frequency Ω writes

$$\Omega = \pm \omega_T \sqrt{\pi - \omega_T^2}, \quad (\text{A1})$$

where ω_T^2 refers to the squared eigenfrequency of the two degenerated translational modes.

The active *Gerris*’s *RT* regimes are condensations of the dynamics on a *RT* plane, defined by the rotation mode and a linear combination of the two translational modes [Fig. 2(d)]. While the two selected modes are also fully delocalized $Q_R = Q_T = 1$, they are not locally orthogonal. This prevents a strict condensation: during the turnarounds, some active force is transformed into mechanical stress of the rigid inner structure, and the polarity field enters inside the circle in the plane of the two selected modes [Figs. 2(d) and 5(a)]. More importantly, the translational and rotation modes are not degenerated [Fig. 2(b)]: tension changes the energy ratio between the two selected modes. Most of the phenomenology can still be understood by studying the dynamics of a single particle trapped in elliptic harmonic potentials [15,37]. As the energy ratio between the two

modes increases, the active particle orbits along circles, ellipses, lemniscates, and higher-order lemniscates [37], the elliptic regimes E_n [15]. In mode space, these limit cycles are more and more condensed along the soft direction. Similarly to the active *Gerris's* RT_n regimes, the E_n regimes are separated by hysteretic and discontinuous transitions. As a final remark, note that the discontinuous transition studied in the main text is thus from an elliptic regime E_1 to a circular one E_0 , standing on planes perpendicular to one another.

*Corresponding author.

olivier.dauchot@espci.fr

†paul.baconnier@espci.fr

- [1] G. H. Koenderink, Z. Dogic, F. Nakamura, P. M. Bendix, F. C. MacKintosh, J. H. Hartwig, T. P. Stossel, and D. A. Weitz, *Proc. Natl. Acad. Sci. U.S.A.* **106**, 15192 (2009).
- [2] S. Henkes, Y. Fily, and M. C. Marchetti, *Phys. Rev. E* **84**, 040301(R) (2011).
- [3] A. M. Menzel and H. Löwen, *Phys. Rev. Lett.* **110**, 055702 (2013).
- [4] L. Berthier and J. Kurchan, *Nat. Phys.* **9**, 310 (2013).
- [5] E. Ferrante, A. E. Turgut, M. Dorigo, and C. Huepe, *Phys. Rev. Lett.* **111**, 268302 (2013).
- [6] J. Prost, F. Jülicher, and J.-F. Joanny, *Nat. Phys.* **11**, 111 (2015).
- [7] P. Ronceray, C. P. Broedersz, and M. Lenz, *Proc. Natl. Acad. Sci. U.S.A.* **113**, 2827 (2016).
- [8] F. G. Woodhouse, H. Ronellenfitsch, and J. Dunkel, *Phys. Rev. Lett.* **121**, 178001 (2018).
- [9] G. Briand, M. Schindler, and O. Dauchot, *Phys. Rev. Lett.* **120**, 208001 (2018).
- [10] F. Giavazzi, M. Paoluzzi, M. Macchi, D. Bi, G. Scita, M. L. Manning, R. Cerbino, and M. C. Marchetti, *Soft Matter* **14**, 3471 (2018).
- [11] N. Klongvessa, F. Ginot, C. Ybert, C. Cottin-Bizonne, and M. Leocmach, *Phys. Rev. Lett.* **123**, 248004 (2019).
- [12] A. Maitra and S. Ramaswamy, *Phys. Rev. Lett.* **123**, 238001 (2019).
- [13] C. Scheibner, A. Souslov, D. Banerjee, P. Surówka, W. T. Irvine, and V. Vitelli, *Nat. Phys.* **16**, 475 (2020).
- [14] P. Baconnier, D. Shohat, C. Hernández López, C. Coulais, V. Démery, G. Düring, and O. Dauchot, *Nat. Phys.* **18**, 1234 (2022).
- [15] See Supplemental Material at <http://link.aps.org/supplemental/10.1103/PhysRevLett.130.028201> for movies, normal mode spectrums, further experimental details, and derivations of the main equations. It includes Refs. [16–19].
- [16] S. Alexander, *Phys. Rep.* **296**, 65 (1998).
- [17] M. Cho, G. R. Fleming, S. Saito, I. Ohmine, and R. M. Stratt, *J. Chem. Phys.* **100**, 6672 (1994).
- [18] S. D. Bembenek and B. B. Laird, *Phys. Rev. Lett.* **74**, 936 (1995).
- [19] L. Wang, A. Ninarello, P. Guan, L. Berthier, G. Szamel, and E. Flenner, *Nat. Commun.* **10**, 26 (2019).
- [20] G. Peyret, R. Mueller, J. d’Alessandro, S. Begnaud, P. Marcq, R.-M. Mège, J. M. Yeomans, A. Doostmohammadi, and B. Ladoux, *Biophys. J.* **117**, 464 (2019).
- [21] C. Chen, S. Liu, X.-q. Shi, H. Chaté, and Y. Wu, *Nature (London)* **542**, 210 (2017).
- [22] H. Xu, Y. Huang, R. Zhang, and Y. Wu, *Nat. Phys.* **1** (2022).
- [23] S. Liu, S. Shankar, M. C. Marchetti, and Y. Wu, *Nature (London)* **590**, 80 (2021).
- [24] K. Bertoldi, V. Vitelli, J. Christensen, and M. Van Hecke, *Nat. Rev. Mater.* **2**, 17066 (2017).
- [25] Y. Kim, H. Yuk, R. Zhao, S. A. Chester, and X. Zhao, *Nature (London)* **558**, 274 (2018).
- [26] E. Siéfert, E. Reyssat, J. Bico, and B. Roman, *Nat. Mater.* **18**, 24 (2019).
- [27] D. B. Liarte, O. Stenull, and T. C. Lubensky, *Phys. Rev. E* **101**, 063001 (2020).
- [28] A. Bossart, D. M. Dykstra, J. van der Laan, and C. Coulais, *Proc. Natl. Acad. Sci. U.S.A.* **118**, e2018610118 (2021).
- [29] X. Yuan, M. Chen, Y. Yao, X. Guo, Y. Huang, Z. Peng, B. Xu, B. Lv, R. Tao, S. Duan *et al.*, *Curr. Opin. Solid State Mater. Sci.* **25**, 100883 (2021).
- [30] C. Bunting and C. C. Eades, *J. Exp. Med.* **44**, 147 (1926).
- [31] J. Kolega, *J. Cell Biol.* **102**, 1400 (1986).
- [32] B. Hinz, D. Mastrangelo, C. E. Iselin, C. Chaponnier, and G. Gabbiani, *Am. J. Pathol.* **159**, 1009 (2001).
- [33] D. E. Ingber, *FASEB J.* **20**, 811 (2006).
- [34] S. Anava, A. Greenbaum, E. B. Jacob, Y. Hanein, and A. Ayali, *Biophys. J.* **96**, 1661 (2009).
- [35] K.-D. N. T. Lam, M. Schindler, and O. Dauchot, *New J. Phys.* **17**, 113056 (2015).
- [36] O. Dauchot and V. Démery, *Phys. Rev. Lett.* **122**, 068002 (2019).
- [37] R. H. Damascena, L. R. E. Cabral, and C. C. de Souza Silva, *Phys. Rev. E* **105**, 064608 (2022).
- [38] A. M. Duval and V. Reiner, *Linear Algebra Appl.* **294**, 259 (1999).
- [39] E. B. Davies, J. Leydold, and P. F. Stadler, *arXiv:math/0009120*.
- [40] G. M. Gladwell and H. Zhu, *Q. J. Mech. Appl. Math.* **55**, 1 (2002).
- [41] R. Bell, P. Dean, and D. Hibbins-Butler, *J. Phys. C* **3**, 2111 (1970).